Hindawi
Concepts in Magnetic Resonance Part B, Magnetic Resonance Engineering
Volume 2024, Article ID 7418643, 10 pages
https://doi.org/10.1155/2024/7418643

Research Article

Impact of Patient Body Posture on RF-Induced Energy Absorption by Orthopedic Plates

Xiaolin Yang,[1] Jianfeng Zheng,[1] Wolfgang Kainz,[2] Xuemin Chen,[3] and Ji Chen[1]

[1]*Department of Electrical and Computer Engineering, University of Houston, Houston, TX 77204-4005, USA*
[2]*HPC for MRI Safety, 210 Lower Grandview Rd, Jasper, GA 30143, USA*
[3]*Department of Engineering, Texas Southern University, Houston, TX, USA*

Correspondence should be addressed to Ji Chen; jchen18@uh.edu

Received 20 February 2024; Revised 1 April 2024; Accepted 17 April 2024; Published 30 April 2024

Academic Editor: Giulio Giovannetti

This study investigates variations in radiofrequency- (RF-) induced energy absorption by orthopedic plates within the human body during 1.5T and 3T magnetic resonance imaging (MRI) scans, considering diverse postures. Using the poseable Duke model, we developed typical postures (O-posture, X-posture, Y-posture, and Z-posture) and placed anatomically correct representations of various orthopedic plates within these postures. Numerical simulations were conducted to evaluate electromagnetic fields and RF-induced energy absorption in these postures near orthopedic plates during MRI scans. Comparing RF-induced energy absorption (peak spatial averaged SAR over 1 g, $pSAR_{1g}$) in postured models to the original posture reveals substantial variations. The $pSAR_{1g}$ differences for X-posture, Y-posture, and Z-posture reach 48%, 134%, and 32% at 1.5T, and 36%, 83%, and 101% at 3T, respectively. Changing posture can lead to higher or lower $pSAR_{1g}$. These findings underscore the impact of patient posture on RF-induced energy absorption in orthopedic plates on the ulna bone. The study recommends considering representative body postures in future evaluations for MR conditional labeling of passive implants. Until then, maintaining a neutral posture during MR scans is advised to mitigate unforeseen RF-induced heating risks.

1. Introduction

Magnetic resonance imaging (MRI) is a safe technique for obtaining high-resolution images of soft tissues inside the human body in a noninvasive manner, without the use of ionizing radiation [1, 2]. To ensure high-quality images of target regions, patients are often instructed to maintain specific postures during MRI scans [3, 4]. However, despite instructions to maintain neutral postures, patients' body conditions and personal habits can lead to some variations in their postures during scans.

Improper postures during MRI scans can lead to severe tissue damage, as evidenced by MRI-related accident reports from the United States Food and Drug Administration (FDA) [5, 6]. For instance, a third-degree burn occurred on the skin of the right hand when it came into contact with the pelvis during an MRI scan, while a second-degree burn occurred on the right elbow when it touched the bore wall of the scanner [7]. Numerical simulations have also confirmed higher radiofrequency (RF)-induced heating due to posture changes [8]. When a closed electrical loop is formed by the patient's body parts, significant local RF-induced energy absorption of up to 500 W/kg of peak spatial-averaged specific absorption rate over 1 gram (peak SAR1 g) can be induced at the contact points under normal operating conditions (with a whole-body averaged specific absorption rate (SAR) of 2 W/kg) [9]. The temperature rise at the contact points between the elbow and the bore wall can exceed 15°C after 1 minute of RF exposure [10]. Variations in patients' postures can result in variations in RF-induced heating by affecting the incident fields inside the human body [11].

While the impacts of postures on RF-induced heating are well-documented, there is a gap in research concerning patients with implantable medical devices. This gap is particularly concerning given that some implants are susceptible to

high RF-induced heating themselves [12–15]. Orthopedic implants are used as examples since they are often positioned on or near movable limbs to treat various bone fractures. Consequently, diverse limb positioning leads to varying postures. Prior studies have addressed safety concerns regarding patients with orthopedic implants during MRI scans [16–22]. The interaction between the RF field generated by the MRI RF coil and metallic implants can result in high local energy absorption, reaching peak SAR_{1g} levels of up to 1000 W/kg near the implants [23]. The extent of RF-induced heating in orthopedic implants is heavily influenced by implant dimensions, orientations, and their location within the patient [24]. According to the American Society for Testing and Materials (ASTM) F-2182 [25], passive implants are placed inside the ASTM phantom to evaluate the RF-induced heating. Based on the simulation and experimental results, conditional requirements (including the input power and scan time) of MRI are restricted to ensure the safety of patients. Due to the limitation of homogeneous phantom [26, 27], the anatomically correct human body model is suggested to assess the RF-induced energy absorption. The human body models with neutral body posture were used in the previous studies [18, 24]. While neutral body postures are often representative, variations in patient posture can alter the field distribution inside the human body, thus significantly impacting RF-induced heating in orthopedic implants. This fluctuation in RF-induced heating results in the varying conditional requirements, posing a substantial safety concern for patients with orthopedic implants, necessitating thorough investigation.

Currently, there are few published studies investigating the impact of patient body posture on RF-induced heating for medical implants [28]. One potential challenge is the development of a diverse set of body postures. On one hand, the human body's flexibility allows for a multitude of postures. On the other hand, creating new body postures is not only complex and time-consuming but also demands significant computational resources and time to simulate the electromagnetic field within the human body with medical implants. As a result, it becomes impractical to assess RF-induced heating across a wide range of postures and implants. Therefore, there is a need to systematically develop a set of typical body posture models based on poseable human body models with an original neutral body posture.

The objective of this study is to develop a set of posture models and evaluate the variation in RF-induced energy absorption of orthopedic implants due to changes in body posture. The methodology involves several steps. First, orthopedic plates of various dimensions are designed to address diverse clinical scenarios. Subsequently, utilizing advanced poseable high-resolution anatomically correct human body models with a neutral posture, a set of postured models is developed to represent patients with orthopedic plates. Following this, numerical simulations are conducted for four imaging landmarks, calculating RF-induced energy absorption based on the simulated electromagnetic field and comparing it across the set of postured models. Finally, the study evaluates the variation in RF-induced energy absorption of orthopedic plates resulting from changes in patient posture.

2. Methods

2.1. Orthopedic Plate Models. Given the arm's flexibility and its potential to result in various postures within an MRI coil, a bridge plate implanted on the ulna bone serves as the representative orthopedic implant in this study. This bridge plate functions to stabilize multifragment fractures of long bones by connecting two pieces of healthy bone, resembling a bridge [29]. In clinical practice, the plate's dimensions are typically determined by the length of the fractured bone to ensure proper screw insertion into healthy bone segments. Generally, no more than half of the plate holes are filled with screws, and multiple plate holes are positioned over each main fracture fragment [30].

This study models a set of orthopedic plates with different dimensions based on clinical conditions. The front and side views of these plates are depicted in Figures 1(a) and 1(b), respectively. Their lengths vary: 140 mm, 120 mm, 100 mm, and 80 mm. Each plate features four screws positioned on its two sides. The plate's width and thickness measure 10 mm and 2 mm, respectively, while the screw's length and diameter are 14 mm and 4 mm, respectively. In simulations, the plate material is assumed to be a perfect electrical conductor (PEC). Although typical material used for implants is stainless steel or titanium, the relative difference in RF-induced energy absorption near device is less than 1% under both 1.5T and 3T [31]. The placement of the plate on the ulna within the human body is illustrated in Figure 1(c).

2.2. Human Posture Models with Orthopedic Plates. To simulate various postures, the poseable advanced high-resolution anatomically correct human body model (Duke) from the virtual population is utilized. The Duke model's original posture, which is also the neutral posture, is depicted in Figures 2 A(1), B(1), and C(1), denoted as "O" (for "Original"). Positioned in the Cartesian coordinate system, the Duke model faces in the y-direction, with the x-direction from right to left and the z-direction from foot to head. Modifications to the body posture are achieved through a computational "poser" tool. Pivoting points are added to the joint locations, enabling adjustments to the arm using the poser tool. Typical postures of concern or interest to researchers and radiologists are selected for investigation.

The accidental shifting of a patient's arm, particularly when it contains implants, towards the MRI bore wall is a cause for concern. In this study, a scenario is considered where an orthopedic plate is placed on the left arm and the arm is horizontally rotated away from the body, resulting in what we refer to as the X-posture. When the human model is in its original posture (O-posture), the horizontal distance between the left arm and the MRI coil is 80 mm. However, as depicted in Figures 2A(2)–2A(4), for human models adopting X-postures (labeled as "X1," "X2," and "X3"), these distances are reduced to 40 mm, 20 mm, and 10 mm, respectively.

Furthermore, a patient's arm may be raised by some objects such as wearing a cast during the MRI scan, which also brings the implants to be closer to the coil. To replicate this scenario, the orthopedic plate is once again positioned

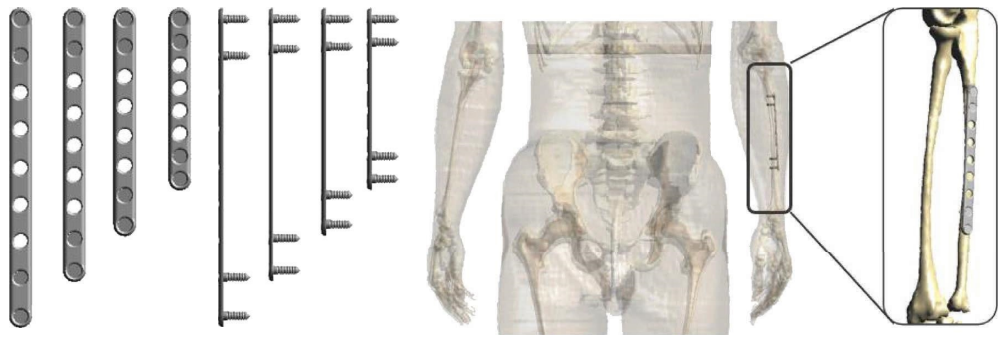

FIGURE 1: Illustration of the orthopedic plate models: (a) the front views, (b) the side views, and (c) placement inside the human body and detailed view of the placement on the ulna.

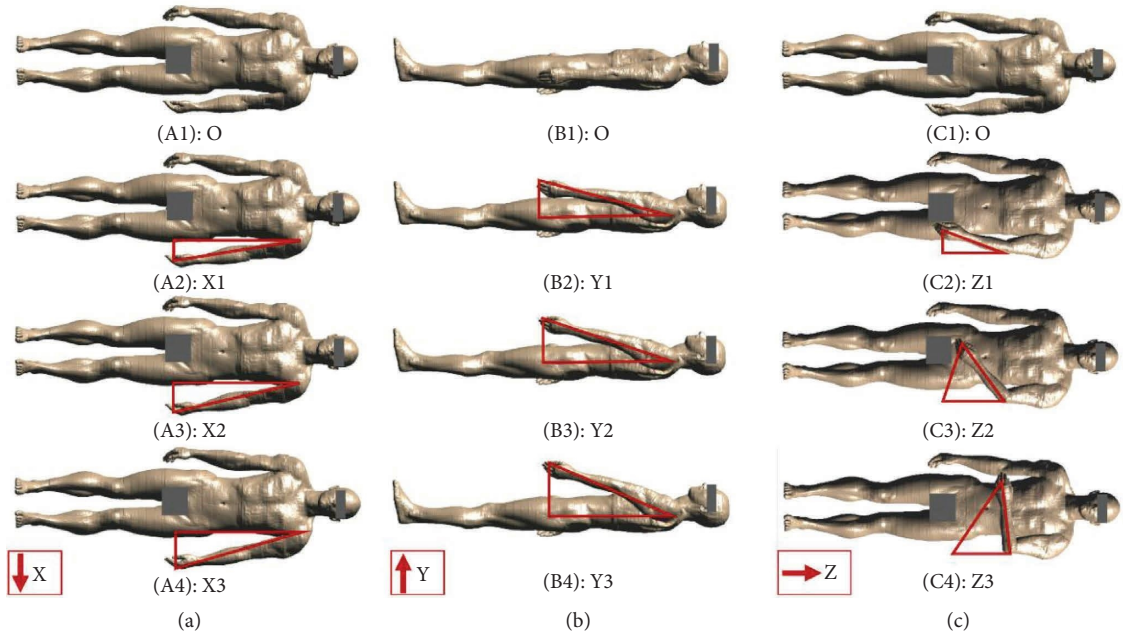

FIGURE 2: Illustrations of the human body models with different postures: (a) Duke model with X-postures X1, X2, and X3, (b) Duke model with Y-postures Y1, Y2, and Y3, and (c) Duke model with Z-postures Z1, Z2, and Z3.

on the ulna, and the entire arm is vertically rotated. In the O-posture model, the vertical distance between the left arm and the coil measures 310 mm. As depicted in Figures 2B(2)–2B(4), the arm-to-coil distances for the Y-posture models, designated as "Y1," "Y2," and "Y3," are 170 mm, 100 mm, and 60 mm, respectively.

Moreover, a previous study has determined that RF-induced heating for implants positioned perpendicular to the axis of the coil, known as the z-axis, is reduced within the ASTM phantom. This behavior of RF-induced heating warrants validation in a human body model. Accordingly, the left arm is rotated 90° above the abdomen to align the plate vertically with the RF coil axis, as depicted in Figure 2C(4). In addition, postures involving a 30° and a 45° rotation are developed, as shown in Figures 2C(2)–2C(3). These rotations adjust the arm's position along the z-direction, denoted as "Z1," "Z2," and "Z3."

After creating the array of postured body models, the orthopedic plates are implanted into these models. To ensure consistent implantation of the orthopedic plate at a fixed position across all posture models, one bounding box is employed for the ulna bone and another bounding box is used to include the orthopedic plate. Across the O-posture, the X-posture, the Y-posture, and the Z-posture models, the relative positions between two bounding boxes remain same in terms of the orientation and the center coordinate.

2.3. Numerical Simulations. A body coil, denoted as G32 [31], with a diameter measuring 630 mm and a length of 650 mm, as depicted in Figure 3(a), serves as the RF source. This coil can produce an RF field identical to that found within a physical MR RF coil, namely, a circularly polarized and uniformly distributed B1 field inside the coil. To power the coil, sixteen voltage sources are positioned at both end

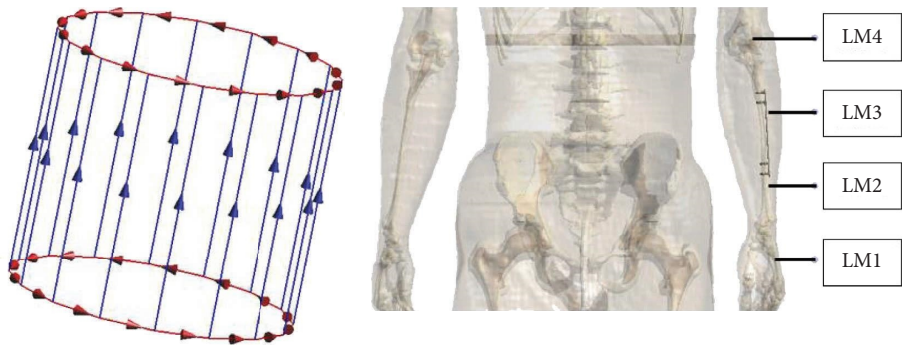

FIGURE 3: Illustration of RF coil and the imaging landmarks: (a) the configuration of the G32 coil and (b) imaging landmarks for the ulna plate inside the human body model.

rings. On each end ring, adjacent sources have a phase delay of 22.5°. In addition, the voltage sources located at the top and bottom rings exhibit opposite phases. All sources operate with the same amplitude. The operational frequency is 64 MHz at 1.5T and 128 MHz at 3T.

Imaging landmark significantly affects RF-induced heating in patients with passive devices [34]. Typically, higher RF-induced heating occurs when the implant resides within the RF coil. Hence, four distinct imaging landmarks are selected for simulation with the ulna plate inside the generic RF coil. The landmark is placed at the isocenter of the coil. As illustrated in Figure 3(b), landmark LM4 for the human body model is positioned at the junction between the humerus and the ulna. Progressing downwards along the z-direction, landmarks LM3, LM2, and LM1 are marked at intervals of 100 mm, spanning 300 mm.

The simulations are conducted using the commercial software SEMCAD X, employing the finite-difference time-domain (FDTD) method. To balance computational time with resolution, the mesh size of the human body model is set at 2 mm. For proper voxelization of the plate, the ulna plate employs a smaller mesh size of 0.7 mm. With approximately 90 million cells, the final computational space achieves a compromise between model resolutions and computational time. The platform for simulations was a Dell XPS desktop with processor of Intel® Core™ i7-6700 and RAM of 16.0 GB. The NVIDIA TESLA C2070 GPU was employed to run the FDTD simulation, and each simulation can be finished in 8 hours. To truncate the simulation domain, the perfectly-matched-layer boundary condition was used to absorb the outgoing electromagnetic signals.

In all results below, we followed the IEC 60601-2-33 to limit the input power using the whole-body (WB) SAR at 2 W/kg or head SAR at 3.2 W/kg for normal operating mode. While the averaged whole-body SAR and head SAR values limit the total input power, the RF-induced heating is inhomogeneous inside the human body and is also closely related to the peak local SAR of 1 g or 10 g [35, 36]. These local SAR are evaluated around a volume of 1 cm cube (1 g peak SAR) or 2.1 cm cube (10 g peak SAR). The local average SAR over 1 gram (SAR1 g) is employed in the study since the device's cross-section is less than 1 cm^2. SAR1 g can be calculated by determining the average SAR within a 1 gram tissue volume.

$$\mathrm{SAR} = \frac{\sigma |E|^2}{2\rho} \tag{1}$$

where σ is the tissue conductivity, ρ is the mass density of the tissue, V is the volume of a mass of 1 gram, and E is the root mean square of E-field strength. The maximum (peak) SAR_{1g} is extracted and denoted as pSAR_{1g}. The pSAR_{1g} is normalized to the limits of the normal operating mode with a whole-body averaged SAR of 2 W/kg based on the SAR limits specified in the International Electrotechnical Commission (IEC) standard 60601-2-33.

3. Results

Comparisons of pSAR_{1g} of orthopedic plates for human body models with original posture and adjusted postures under 1.5T and 3T MRI systems are presented as follows.

3.1. RF-Induced Energy Absorption at 1.5T. At 1.5T, the pSAR_{1g} near the orthopedic plates with different dimensions inside the human postured body models is shown in Figure 4.

With changes in imaging landmarks, the peak SAR averaged over 1 gram (pSAR_{1g}) decreases for both the O-posture and the X-posture across all orthopedic plates in Figures 4(A1)–4(D1). However, the reduction of pSAR_{1g} is more pronounced for the X-posture compared to the O-posture. Notably, in comparison to the O-posture, the pSAR_{1g} of the X-posture is higher at LM1 but lower at the other three landmarks. This observation suggests that as the patient's left arm approaches the coil, the imaging landmarks can have a larger impact on the RF-induced heating.

In Figures 4(A2)–4(D2), the trends observed for the Y-posture differ from those of the O-posture as the imaging landmark is altered. Typically, the pSAR_{1g} shows a pattern of initial decrease followed by an increase, with its minimum occurring at LM2 or LM3 and its maximum at LM4. Substantial disparities in pSAR_{1g} between the O-posture and the Y-posture are evident. Notably, for a patient with an

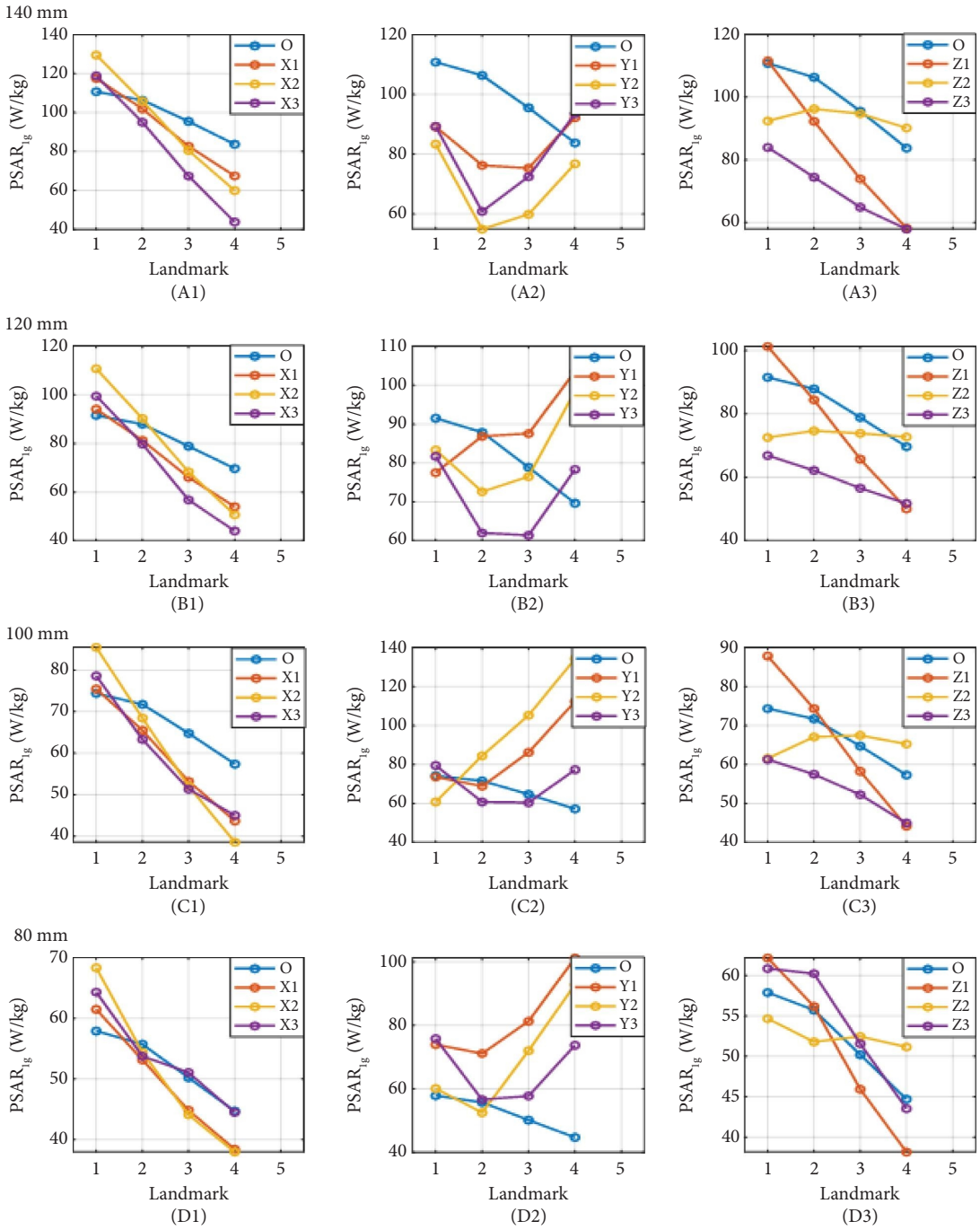

FIGURE 4: Comparison of $pSAR_{1g}$ for various orthopedic plates inside the human models with different postures for four imaging landmarks at 1.5T. (A1)–(A3): Comparison of the $pSAR_{1g}$ for the orthopedic plates with a length of 140 mm. (B1)–(B3): Comparison of the $pSAR_{1g}$ for the orthopedic plates with a length of 120 mm. (C1)–(C3): Comparison of the $pSAR_{1g}$ for the orthopedic plates with the length of 100 mm. (D1)–(D3): Comparison of the $pSAR_{1g}$ for the orthopedic plates with the length of 80 mm.

orthopedic plate measuring 140 mm in length, the $pSAR_{1g}$ decreases from 106 W/kg to 55 W/kg when transitioning from the O-posture to the Y2-posture at LM2, as illustrated in Figure 4(A2). Conversely, for a patient with an orthopedic plate measuring 100 mm in length, the $pSAR_{1g}$ increases from 57 W/kg to 134 W/kg at LM4 when adopting the Y2-posture instead of the O-posture, as depicted in Figure 4(C2). When the patient's left arm is raised, the RF-induced energy absorption for the orthopedic plate can increase by 77 W/kg or decrease by 51 W/kg, with its magnitude highly dependent on the height of the raised arm and the dimensions of the orthopedic plate.

As shown in Figure 4(D3), the $pSAR_{1g}$ values exhibit a decrease in the Z1-posture, and the Z3-posture as the imaging landmark is altered. Particularly, the $pSAR_{1g}$ for the Z1-posture demonstrates a more significant reduction

compared to that of the O-posture. Moreover, for all orthopedic plates except the one measuring 80 mm in length, the $pSAR_{1g}$ of the Z3-posture is lower than that of the O-posture. In contrast, the variations in $pSAR_{1g}$ for the Z2-posture remain within 10 W/kg across changes in the imaging landmark. When the orthopedic plate is perpendicular to the coil axis, altering the patient's posture can lead to a substantial variation in RF-induced energy absorption, especially for orthopedic plates with dimensions ranging from 100 mm to 140 mm.

3.2. RF-Induced Energy Absorption at 3 T. At 3 T, the $pSAR_{1g}$ of the orthopedic plates with different dimensions inside human posture models is shown in Figure 5.

The X-posture generally results in a reduction in the $pSAR_{1g}$ for all orthopedic plates across all four imaging landmarks. However, there are three exceptions to this trend: (1) the X2-posture for the 140 mm plate at LM1, as depicted in Figure 5(A1); (2) the X2-posture; and (3) the X3-posture for the 120 mm plate at LM1, as shown in Figure 5(B1). The most significant increase in $pSAR_{1g}$ can reach up to 20 W/kg, occurring for the 140 mm plate in the X2-posture at landmark LM1. When the patient's left arm approaches the coil, RF-induced energy absorption for the orthopedic plate can generally be reduced during MRI scans from landmark LM2 to LM4. However, exceptions to this reduction may occur in certain scenarios, as indicated by the examples mentioned above.

With the change of imaging landmark, the $pSAR_{1g}$ of the O-posture increases first and then decreases as shown in Figures 5(A2)–5(D2). Conversely, for the Y-posture, the $pSAR_{1g}$ decreases, with the highest and lowest values observed at landmarks LM1 and LM4, respectively. When transitioning from the O-posture to the Y-posture, the $pSAR_{1g}$ can either increase from 57 W/kg to 99 W/kg at LM1 or decrease from 77 W/kg to 16 W/kg at LM4. These findings suggest that as the patient's left arm is raised, RF-induced energy absorption for the orthopedic plate increases at LM1, remains relatively constant at LM2, and decreases at LM3 and LM4.

Figures 5(A3)–5(D3) illustrate that the Z-posture tends to increase the $pSAR_{1g}$ of orthopedic plates. However, as the imaging landmark changes, the $pSAR_{1g}$ decreases for the Z-posture, resulting in reduced differences in $pSAR_{1g}$ between the Z-posture and the O-posture. Particularly at landmark LM1, the $pSAR_{1g}$ for the Z-posture can be up to 2 times higher than that for the O-posture for plates measuring 140 mm and 100 mm in length. When the patient's left arm is perpendicular to the coil axis, the RF-induced energy absorption increases.

3.3. Relative Difference. From the results above, patients' postures can significantly affect the RF-induced energy deposited near orthopedic plates. The variation in RF-induced energy near orthopedic plates depends on the type of posture, the dimensions of the orthopedic plate, and the operating frequency of the MRI system. To quantitatively illustrate the variation of $pSAR_{1g}$ for the orthopedic plate caused by different postures, the relative difference of $pSAR_{1g}$ between O-posture and each posture are calculated (all the relative differences are in Supplementary Materials 1). The maximal relative difference of $pSAR_{1g}$ between the O-posture and X, Y, and Z postures for 1.5T and 3T MRI systems are shown in Tables 1 and 2, respectively. Notably, the highest relative difference of $pSAR_{1g}$ for various orthopedic plates is observed for the Y-posture at 1.5T and the Z-posture at 3T. At 3T, the Z-posture increases the $pSAR_{1g}$ substantially for the orthopedic plate for all imaging landmarks, which can become a significant safety concern. At 1.5T, the effect of the Y-posture on the $pSAR_{1g}$ depends much on the length of the orthopedic plates. For a long orthopedic plate, such as the 140 mm plate, the Y-posture often reduces the $pSAR_{1g}$. However, the $pSAR_{1g}$ for a short orthopedic plate will increase significantly for the Y-posture. In addition, the X-posture also has a non-negligible effect on the $pSAR_{1g}$ for orthopedic plates with a relative difference up to 48% and 36% for 1.5T and 3T MR systems, respectively.

4. Discussion

The variations in $pSAR_{1g}$ are caused by patient posture because the incident RF field in the vicinity of the orthopedic plate changes due to the arm movement. The electromagnetic field distributions are simulated for patients with different postures after removing orthopedic plates. At landmark LM4, the magnitude of E-field distributions for the four postures is compared with the O-posture at both 1.5T and 3T, as shown in Figure 6. For the X3, Y2, and Z3 postures, the lower magnitude of E-field inside the forearm is observed compared with that for O-posture, resulting in the decrease of $pSAR_{1g}$ for the plate.

Among the human posture models examined in this study, the variation of $pSAR_{1g}$ for the orthopedic plate reaches up to 100% compared to the original posture. Such significant variation will result in varying conditional requirements (input power and scan time) of the MRI, indicating that conditional requirements under neutral posture do not guarantee the safety of patients. It is strongly recommended that patients maintain a consistent neutral posture during MRI examinations to mitigate potential risks of unexpected heating, which may not have been accounted for during the determination of MRI conditional labeling. In addition, it highlights that the original posture may not represent the worst-case scenario when assessing RF-induced heating for orthopedic plates within the human body model. Conducting comprehensive studies involving various postures is essential, with further research needed to identify the posture that presents the highest risk. Furthermore, the RF-induced energy absorption could potentially be reduced by adopting specific postures, such as the Z3-posture in 1.5T and X1-posture in 3T. However, this observation is specific to the plate and human body model utilized in this study. Additional research is warranted to elucidate the underlying mechanisms, potentially guiding the way for clinical applications aimed at preventing tissue heating damage caused by orthopedic plates.

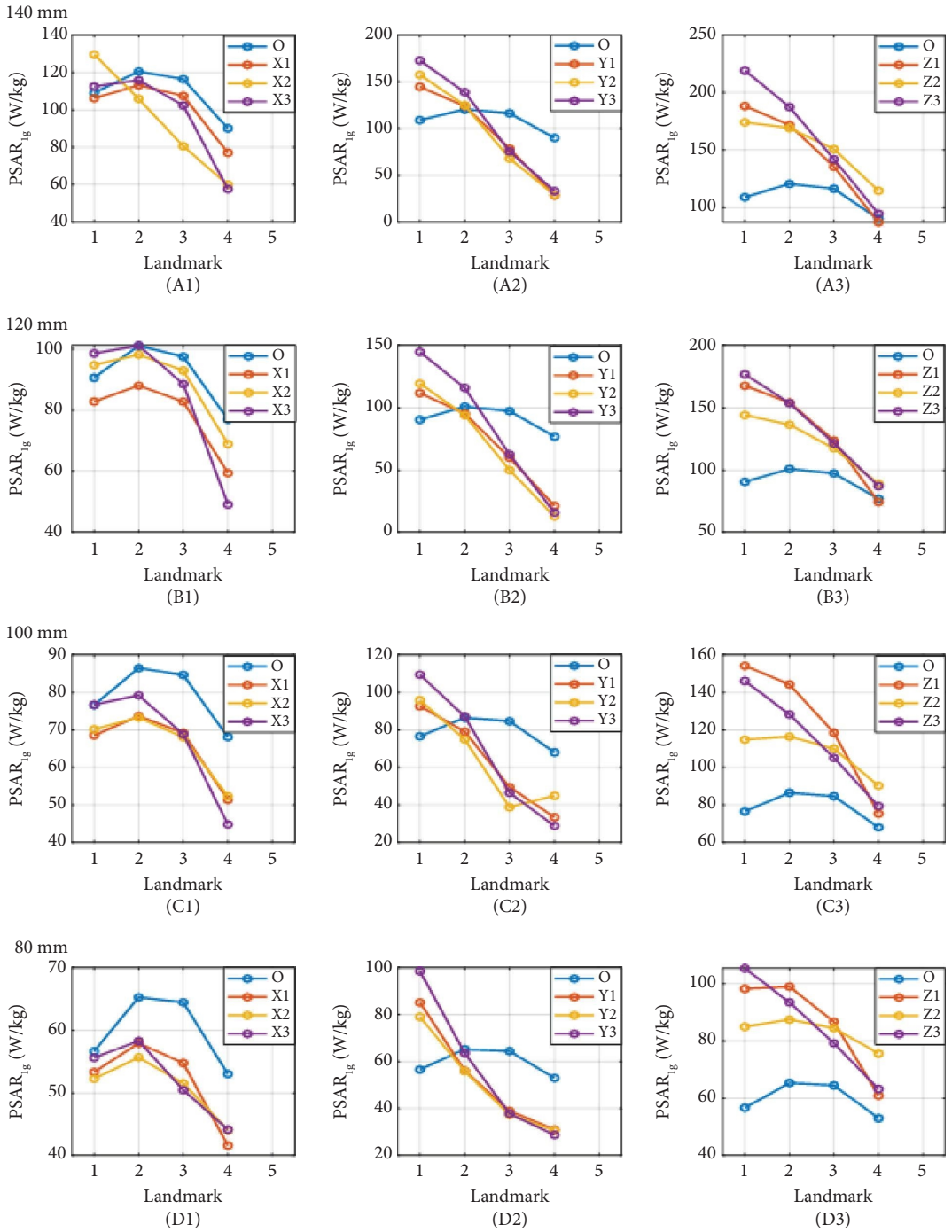

Figure 5: Comparison of the $pSAR_{1g}$ for various orthopedic plates inside the human models with different postures for four imaging landmarks at 3T. (A1)–(A3): Comparison of the $pSAR_{1g}$ for the orthopedic plates with a length of 140 mm. (B1)–(B3): Comparison of the $pSAR_{1g}$ for the orthopedic plates with a length of 120 mm. (C1)–(C3): Comparison of the $pSAR_{1g}$ for the orthopedic plates with a length of 100 mm. (D1)–(D3): Comparison of the $pSAR_{1g}$ for the orthopedic plates with a length of 80 mm.

Table 1: The maximal relative difference for the $pSAR_{1g}$ between the O-posture and other postures for various orthopedic plates at 1.5T.

	X (%)	Y (%)	Z (%)
140 mm	48	48	32
120 mm	37	49	29
100 mm	33	134	23
80 mm	18	126	15

Table 2: The maximal relative difference of $pSAR_{1g}$ between the O-posture and other postures for various orthopedic plates at 3T.

	X (%)	Y (%)	Z (%)
140 mm	36	68	101
120 mm	36	83	96
100 mm	34	58	101
80 mm	22	74	86

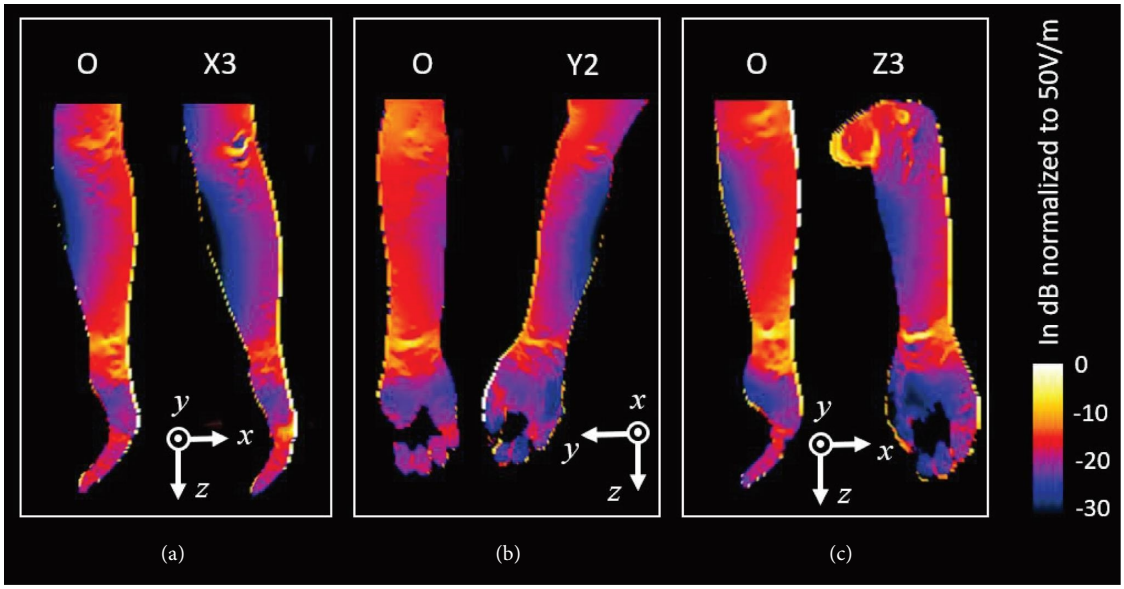

Figure 6: Comparisons of the E-field distribution near the ulna bone for the human body model with different postures and the original posture: (a) X3 posture at 1.5T, (b) Y2 posture at 3T, and (c) Z3 posture at 1.5T.

5. Conclusion

This study investigated the RF-induced energy absorption of orthopedic plates with various dimensions within human models, considering both the original posture and a range of typical body postures for both 1.5T and 3T MR systems. Significant variations in RF-induced energy absorption were observed across different postures. Specifically, at 1.5T, the relative differences in $pSAR_{1g}$ for the X-posture, Y-posture, and Z-posture were 48%, 134%, and 32%, respectively. At 3T, these differences were 36%, 83%, and 101%, respectively. It is noticed that three postures studied in this paper had a notable impact on the $pSAR_{1g}$ of the orthopedic plates, indicating the need to prioritize these postures when assessing RF-induced heating. The distribution of the electric field (E-field) significantly changes when the patient's arms are repositioned, resulting in variations in $pSAR_{1g}$ for the orthopedic plates. Thus, considering various posture models is crucial when evaluating RF-induced heating for passive implants to mitigate unexpected heating risks. At present, posture variations are not typically factored into the standard assessment of RF-induced heating for MR conditional labeling of passive implants. Further research is necessary to explore special postures that may result in maximal or minimal RF-induced heating. Given the observed disparities in $pSAR_{1g}$ in our study, we recommend that patients maintain a consistent posture during MRI scans.

Data Availability

The data used to support the findings of this study are available in the supplementary materials of this article.

Conflicts of Interest

The authors declare that they have no conflicts of interest.

Acknowledgments

This work was supported by the National Science Foundation [grant 1922389].

Supplementary Materials

All the relative differences for the $pSAR_{1g}$ between the O-posture and other postures for various orthopedic plates at 1.5T and 3T are calculated to support the maximum relative difference. (*Supplementary Materials*)

References

[1] A. Kangarlu and P.-M. L. Robitaille, "Biological effects and health implications in magnetic resonance imaging," *Concepts in Magnetic Resonance*, vol. 12, no. 5, pp. 321–359, 2000.

[2] J. S. van den Brink, "Thermal effects associated with RF exposures in diagnostic MRI: overview of existing and emerging

concepts of protection," *Concepts in Magnetic Resonance: Part A B*, vol. 2019, Article ID 9618680, 17 pages, 2019.

[3] M. Friedrich, "MRI of the breast: state of the art," *European Radiology*, vol. 8, no. 5, pp. 707–725, 1998.

[4] V. V. Patel, K. S. Hall, M. D. Ries et al., "A three-dimensional MRI analysis of knee kinematics," *Journal of Orthopaedic Research: Official Publication of the Orthopaedic Research Society*, vol. 22, no. 2, pp. 283–292, 2004.

[5] J. G. Delfino, D. M. Krainak, S. A. Flesher, and D. L. Miller, "MRI-related FDA adverse event reports: a 10-yr review," *Medical Physics*, vol. 46, no. 12, pp. 5562–5571, 2019.

[6] M. F. Dempsey and B. Condon, "Thermal injuries associated with MRI," *Clinical Radiology*, vol. 56, no. 6, pp. 457–465, 2001.

[7] W. A. Kudrle, P. A. Narayana, and H. A. Dunsford, "Magnetic resonance imaging of burn injury in rats," *Magnetic Resonance Imaging*, vol. 9, no. 4, pp. 533–543, 1991.

[8] X. Yang, J. Zheng, and Ji Chen, "Impacts of the arm and leg postures on the RF-induced heating for the human body under MRI," in *Proceedings of the 2020 IEEE International Symposium on Electromagnetic Compatibility & Signal/Power Integrity (EMCSI)*, Reno, NV, USA, July 2020.

[9] X. Yang, J. Zheng, Yu Wang, S. A. Long, W. Kainz, and Ji Chen, "Bodyloop related MRI radiofrequency-induced heating hazards: observations, characterizations, and recommendations," *Magnetic Resonance in Medicine*, vol. 87, no. 1, pp. 337–348, 2021.

[10] M. Tang, K. Okamoto, T. Haruyama, and T. Yamamoto, "Electromagnetic simulation of RF burn injuries occurring at skin-skin and skin-bore wall contact points in an MRI scanner with a birdcage coil," *Physica Medica*, vol. 82, pp. 219–227, 2021.

[11] F. G. Shellock, "Radiofrequency energy-induced heating during MR procedures: a review," *Journal of Magnetic Resonance Imaging*, vol. 12, no. 1, pp. 30–36, 2000.

[12] L. Winter, E. Oberacker, C. Özerdem et al., "On the RF heating of coronary stents at 7.0 tesla MRI," *Magnetic Resonance in Medicine*, vol. 74, no. 4, pp. 999–1010, 2014.

[13] M. Hasegawa, K. Miyata, Y. Abe, and T. Ishigami, "Radiofrequency heating of metallic dental devices during 3.0 T MRI," *Dentomaxillofacial Radiology*, vol. 42, no. 5, 2013.

[14] K. Fujimoto, L. M. Angelone, E. Lucano, S. S. Rajan, and M. I. Iacono, "Radio-frequency safety assessment of stents in blood vessels during magnetic resonance imaging," *Frontiers in Physiology*, vol. 9, 2018.

[15] J. Zheng, M. Xia, W. Kainz, and Ji Chen, "Wire-based sternal closure: MRI-related heating at 1.5 T/64 MHz and 3 T/128 MHz based on simulation and experimental phantom study," *Magnetic Resonance in Medicine*, vol. 83, no. 3, pp. 1055–1065, 2019.

[16] Y. Liu, Ji Chen, F. G. Shellock, and W. Kainz, "Computational and experimental studies of an orthopedic implant: MRI-related heating at 1.5-T/64-MHz and 3-T/128-MHz," *Journal of Magnetic Resonance Imaging*, vol. 37, no. 2, pp. 491–497, 2012.

[17] A. Arduino, U. Zanovello, J. Hand et al., "Heating of hip joint implants in MRI: the combined effect of RF and switched gradient fields," *Magnetic Resonance in Medicine*, vol. 85, no. 6, pp. 3447–3462, 2021.

[18] J. Powell, A. Papadaki, J. Hand, A. Hart, and D. McRobbie, "Numerical simulation of SAR induced around Co-Cr-Mo hip prostheses in situ exposed to RF fields associated with 1.5 and 3 T MRI body coils," *Magnetic Resonance in Medicine*, vol. 68, no. 3, pp. 960–968, 2011.

[19] I. Khodarahmi, S. Rajan, R. Sterling, K. Koch, J. Kirsch, and J. Fritz, "Heating of hip arthroplasty implants during metal artifact reduction MRI at 1.5- and 3.0-T field strengths," *Investigative Radiology*, vol. 56, no. 4, pp. 232–243, 2020.

[20] J. Wooldridge, A. Arduino, L. Zilberti et al., "Gradient coil and radiofrequency induced heating of orthopaedic implants in MRI: influencing factors," *Physics in Medicine and Biology*, vol. 66, no. 24, 2021.

[21] A. Arduino, O. Bottauscio, M. Chiampi, U. Zanovello, and L. Zilberti, "A contribution to MRI safety testing related to gradient-induced heating of medical devices," *Magnetic Resonance in Medicine*, vol. 88, no. 2, pp. 930–944, 2022.

[22] L. Zilberti, A. Arduino, R. Torchio et al., "Orthopedic implants affect the electric field induced by switching gradients in MRI," *Magnetic Resonance in Medicine*, vol. 91, no. 1, pp. 398–412, 2024.

[23] R. Guo, J. Zheng, Yu Wang et al., "Computational and experimental investigation of RF-induced heating for multiple orthopedic implants," *Magnetic Resonance in Medicine*, vol. 82, no. 5, pp. 1848–1858, 2019.

[24] M. Xia, J. Zheng, and J. Chen, "Numerical study on MRI RF-induced heating for the trauma screw implanted in three human models," in *Proceedings of the 2020 IEEE International Symposium on Electromagnetic Compatibility & Signal/Power Integrity (EMCSI)*, Reno, NV, USA, August 2020.

[25] American Society for Testing and Materials International, *Standard Test Method for Measurement of Radio Frequency Induced Heating on or Near Passive Implants during Magnetic Resonance Imaging*, American Society for Testing and Materials International, West Conshohocken, PE, USA, 2019.

[26] R. Guo, M. Chen, J. Zheng, R. Yang, Ji Chen, and W. Kainz, "Comparison of In-Vivo and In-Vitro MRI RF Heating for Orthopedic Implant at 3 Tesla," in *Proceedings of the 2017 IEEE International Symposium on Antennas and Propagation and USNC/URSI National Radio Science Meeting*, San Diego, CA, USA, August 2017.

[27] R. Guo, J. Zheng, Ji Chen, and W. Kainz, "RF-induced Heating Comparison between In-Vivo and In-Phantom for 1.5T MRI," in *Proceeding of the 2016 IEEE International Symposium on Electromagnetic Compatibility (EMC)*, Ottawa, Canada, July 2016.

[28] X. Yang, R. Guo, J. Zheng, and Ji Chen, "RF-induced heating for cardiac rhythm management (CRM) in patients with different postures," in *Proceeding of the 2022 IEEE International Symposium on Electromagnetic Compatibility & Signal/Power Integrity (EMCSI)*, Spokane, WA, USA, August 2022.

[29] "ORIF- bridge plating for segmental, fragmentary, middle 1/3 fractures," https://surgeryreference.aofoundation.org/orthopedic-trauma/adult-trauma/femoral-shaft/segmental-fragmentary-middle-1-3-fractures/orif-bridge-plating.

[30] Plating, https://surgeryreference.aofoundation.org/orthopedic-trauma/adult-trauma/basic-technique/basic-principles-of-plating#compression-plating.

[31] L. Zilberti, U. Zanovello, A. Arduino, O. Bottauscio, and M. Chiampi, "RF-Induced heating of metallic implants simulated as PEC: is there something missing?" *Magnetic Resonance in Medicine*, vol. 85, no. 2, pp. 583–586, 2020.

[32] M. C. Gosselin, E. Neufeld, H. Moser et al., "Development of a new generation of high-resolution anatomical models for medical device evaluation: the Virtual Population 3.0," *Physics in Medicine and Biology*, vol. 59, no. 18, pp. 5287–5303, 2014.

[33] E. Lucano, M. Liberti, G. G. Mendoza et al., "Assessing the electromagnetic fields generated by a radiofrequency MRI

body coil at 64 MHz: defeaturing versus accuracy," *IEEE Transactions on Biomedical Engineering*, vol. 63, no. 8, pp. 1591–1601, 2016.

[34] M. Xia, J. Zheng, R. Yang et al., "Effects of patient orientations, landmark positions, and device positions on the MRI RF-induced heating for modular external fixation devices," *Magnetic Resonance in Medicine*, vol. 85, no. 3, pp. 1669–1680, 2020.

[35] "Assessment of radiofrequency-induced heating in the magnetic resonance (MR) environment for multi-configuration passive medical devices," *Guidance for Industry and Food and Drug Administration Staff*.

[36] IEC, *International Standard, Medical Equipment Part 2-33: Particular Requirements for the Safety of Magnetic Resonance Equipment for Medical Diagnosis*, International Electrotechnical Commission, Geneva, Switzerland, 3rd edition, 2022.